CAAI Transactions on Intelligence Technology

Research Article

Automated segmentation technique with self-driven post-processing for histopathological breast cancer images

ISSN 2468-2322
Received on 2nd December 2019
Revised on 22nd May 2020
Accepted on 14th July 2020
doi: 10.1049/trit.2019.0077
www.ietdl.org

Chetna Kaushal, Anshu Singla ✉

Chitkara University Institute of Engineering and Technology, Chitkara University, Punjab, India
✉ *E-mail: anshu.singla@chitkara.edu.in*

Abstract: Automated segmentation of histopathological images is a challenging task to detect cancerous cells in breast tissue. Recent reviews state high accuracy to segment image, but depends on user input, say window area size, time steps, level set, magnification factor and so on. To extract the region of interest effectively, the subject expert performs post-processing operations several times on the segmentation results with different input values for different parameters say, area opening, fill holes and selects most appropriate enhanced image required for further analysis. The authors proposed an automated segmentation technique followed by self-driven post-processing operations to detect cancerous cells effectively. The post-processing method itself determines the value of different parameters for different operations based on segmented results obtained. The proposed technique has the following features: (i) technique is context sensitive; (ii) no prior setting of time step, weighted area coefficient parameters is required; (iii) magnification independent; (iv) post-processing operations are self-driven which enhance segmentation results adaptively. The experimental results are compared with four state-of-the-art techniques: fuzzy C-means, spatial fuzzy C-means, spatial neutrosophic distance regularised level set and convolutional neural network-based PangNet. Experimental results obtained on two publicly available data sets show that the proposed technique outperforms effectively.

1 Introduction

The development of digital slide scanners has led to digitise the histopathological slides and store them in the form of a digital image that can be analysed by the pathologists repetitively [1]. Information present in the tissue is differentiated by staining to ease the visual interpretation. Haematoxylin and Eosin (H&E) staining is the most common staining method where Haematoxylin dyes the nuclei in a dark blue colour while Eosin dyes cytoplasm in pink colour that facilitates nuclei analyses [2]. The manual diagnosis by pathologists from the sample of stained tissue is a very challenging task as it takes a lot of time and may lead to inter- and intra-observer variabilities. Advances and automation in computer technology have fascinated the attention of many researchers in the field of medical imaging [3, 4]. This advancement is boon to pathologists in rapid analysis of region-of-interest in images with precision and enhances the effective diagnosis. One of the dominant reasons of death amongst women is breast cancer [5]. Due to the complicated and varied structure of the breast tissue, histopathological analysis is the inexorable and best method to affirm cancer [6]. The automated cancer detection techniques using histopathology remains a challenge [7]. Therefore, automatic techniques to pre-process and segment the digital histopathological images can be a remarkable notch to reduce the mortality rate. Pre-processing of an acquired image leads to enhancement of its quality by the elimination of noise and unwanted regions [8]. The clustered and touching nuclei in tissues of the histopathological images need to be separated from the background in order to effectively diagnose breast cancer. The key challenge is to identify all the cancerous cells accurately by enhancing the image quality but preserving the texture details without using any human intervention [9].

In general, the segmentation techniques to segment cells and nuclei are based on thresholding [10–15], active contours [16–18], clustering [19–21], region growing [22], watershed segmentation [23, 24], or hybridisation of these techniques [25–27]. The key challenge the aforementioned techniques encounter is over- and under-segmentation problems due to variability within the cell nuclei present in the image [28]. Wang *et al.* [13] identified mitosis in breast histopathological images using the thresholding technique based on cascaded approach with convolutional neural network (CNN) model. Kowal *et al.* [14] presented a technique of adaptive thresholding to perform segmentation on breast histopathological images that tend to differentiate the malignant tumours from the benign ones. Abdolhoseini *et al.* [15] introduced a local adaptive thresholding algorithm employing watershed regions to split nuclei that are heavily clustered due to variations in intensity. The algorithm is dependent on the parameter of object size which is to be set by the user. Wang *et al.* [22] presented the region growing-based technique that solved the problem of heterogeneity within the cells to some level. This technique could not handle the overlapping and touching cell nuclei. To decrease the problem of over-segmentation, the marker-controlled watershed algorithm was employed in the cell nuclei segmentation [23]. Qu *et al.* [24] presented an automated algorithm with marker controlled watershed that relies on morphological features extraction to form a classification model to predict breast cancer. The marker detection technique lacks in identifying the count of targets within a region resulting in making one target to have more than one marker. Hence, still face the problem of over-segmentation. Active contour models (ACMs) are used for edge detection, tracking objects, and medical image analysis. Mouelhi *et al.* [16] introduced ACM to segment the cell nuclei in combination with an enhanced watershed method to segment breast cancer images. Ali and Madabhushi [17] presented a region-based segmentation by employing ACM to segment the nucleus and glandular structures. These techniques are initialisation sensitive and cannot separate overlapping nuclei without further post-processing the images. Xu *et al.* [18] proposed a convolutional model that included ACM with ellipse fitting to overcome the overlapping problem in clustered nuclei. Sornapudi *et al.* [19] investigated a deep learning technique by

This is an open access article published by the IET, Chinese Association for Artificial Intelligence and Chongqing University of Technology under the Creative Commons Attribution -NonCommercial License (http://creativecommons.org/licenses/by-nc/3.0/)

generating super pixels using a clustering algorithm for nuclei segmentation. Only the local information was gathered by the super pixel generation. In clustering techniques [19–21], the number of clusters to be defined for a complex image is a challenging task and these are sensitive to variations of intensity in the cell nuclei. Medical image analysis using neutrosophic techniques also require several parameters initialisation like the initial level set, time step, weighting coefficient, weighted area [29]. Vahadane and Sethi [25] used hybrid of Otsu thresholding and watershed technique to control the problem of over-segmentation. The technique adopted fast radial symmetry transform to generate foreground seeds and enhanced image by Otsu thresholding and further removed false detections applying logical operations. Husham *et al.* [26] introduced a different hybridised technique that relies on Otsu thresholding and level set to detect nuclei and implement segmentation. Zhao *et al.* [27] integrated framework of deep learning with ACM to deal with the overlapping nuclei. Li *et al.* implemented refinenet framework based on CNN to segment whole-slide breast images. A segmentation accuracy of only 75.5% was achieved due to class imbalance in the data set [30]. Mejbri *et al.* [31] employed deep neural network for tissue-level segmentation for 11 H&E stained breast cancer histological images of their own data set.

Once the segmented image is obtained, post-processing is applied to enhance the image for analysis. For this enhancement, different morphological operations are applied [32]. In the literature, morphological operations inputs are generally hit and trial or subjective to radiologist's experience/analysis. There are no fixed input values for structuring element, area opening etc. Kaushal *et al.* [9] presented a technique that is more suitable for ellipse-shaped nuclei and may not work well if the nuclei is not elliptical in shape which may cause over-segmentation problem. This technique is sensitive when the radius of the structuring element has a value smaller than 8 as structuring element size was fixed to value 7. Pan *et al.*'s method to segment the nuclei in pathological images followed by a series of morphological operations. The authors introduced some prior knowledge in morphological cleaning, opening operation by specified area value to improve the segmentation performance [33]. Chekkoury *et al.* [34] removed the noise from the histopathological images during post-processing using specific values for morphological dilation followed by an erosion operation to obtain the nuclei boundary. Krishnan *et al.* [35] removed the unwanted regions in histopathological images employing morphological closing operation followed by opening with a disk-shaped structuring element. Rezaei *et al.* [36] performed the morphological operations on the binary map with user input values for de-noising and filling the holes to acquire a solid segmentation map. The several runs to determine the values of the structuring elements, hole fill, area opening etc. is time-consuming and requires awareness of image analysis techniques for the radiologist. This process of judgement of appropriate input values can be reduced if post-processing operations are completely automatic, i.e. based on segmented results obtained the parameters are computed automatically.

Based on the aforementioned literature, a segmentation technique is required that overcomes the above-mentioned problems to effectively segment the cells from the histopathological images of breast cancer. The authors in this paper have proposed an automatic segmentation technique, which is followed by self-driven post-processing operations that automatically compute the input values for morphological operations during post-processing based on the segmented results obtained. The proposed technique computes one-dimensional energy curve [37] which includes neighbourhood information, which may reduce the over-segmentation and under-segmentation problems effectively. Based on the energy curve, tending thresholds are determined to find a region of interest in a breast cancer histopathological image. An entropy for each tending threshold is calculated and the threshold with maximum entropy is selected as the favourable threshold. This favourable threshold segments the image by classifying it into cell nuclei that are the target region and background regions. The proposed technique is independent of magnification and does not require any initial setting of time step, area weight parameter. It comprises of self-driven post-processing operations that improve the structural similarity of the cells in the segmented image. An improvement in structural similarity leads to significant qualitative and quantitative results. Experimental results of the proposed technique on different metrics have been compared with a traditional fuzzy C-means (FCM) technique, two recently developed segmentation techniques: spatial fuzzy C-means (SFCM), spatial neutrosophic distance regularised level set (SNDRLS), and a deep learning model: PangNet, in order to analyse its effectiveness. The proposed and existing state-of-the-art techniques are implemented on two breast cancer data sets [38, 39].

This paper is organised into four sections: Section 2 describes the proposed technique. Section 3 consists of the experimental results and their analysis. The conclusion of the work presented in this paper is discussed in Section 4.

2 Proposed technique

An automated segmentation technique followed by self-driven post-processing operations is proposed in this research paper. The proposed technique is divided into three major steps:

(i) *Pre-processing:* To smoothen the image.
(ii) *Automated segmentation:* Thresholding to identify the region of interest accurately.
(iii) *Self-driven post-processing:* To improve the structural similarity.

A detailed discussion of each step is discussed in the subsequent subsections.

2.1 Pre-processing

A huge number of variations occur while image acquisition and slide preparation. The brightness in the background of the captured histopathological image is generally not uniform due to the compressing process. The cell nuclei in histopathological images need to be identified for accurate segmentation of cancerous cells. Thus, few pre-processing steps are essential to smooth the pixels and enhance the contrast for better overall visual distinction between the cell nuclei (target region) and background (intercellular matter).

2.1.1 Convert histopathological image to grey image: Pathologists have to focus on the identification of the cell nuclei. The acquired RGB format image is shown in Fig. 1*a* is initially converted into a grey image as shown in Fig. 1*b*.

2.1.2 Apply median filter to smooth the pixels in the image: To reduce the noise while image acquisition, a median filter is used to smooth the pixels in the image while preserving its edges. Assume $A = \left(1 \le i \le r, 1 \le j \le s\right)$ is an image of size $(r \times s)$ with the grey value g_{ij} of the image A at $\left(i, j\right)$ the position of the pixel. Each output pixel of image A includes the median value in a 3×3 square neighbourhood as written in (1) around the corresponding pixel in the input image A.

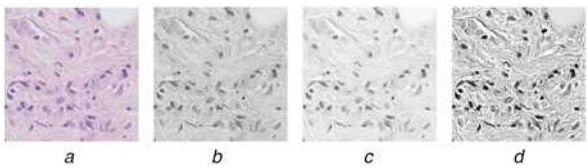

Fig. 1 *Different images obtained during pre-processing steps*

a Histopathological Image
b Grey Image
c Median filter output
d Bottom–top hat filter output

This is an open access article published by the IET, Chinese Association for Artificial Intelligence and Chongqing University of Technology under the Creative Commons Attribution -NonCommercial License (http://creativecommons.org/licenses/by-nc/3.0/)

$$g_i' = \text{median}\Big\{g_{i,j}, g_{i+1,j}, g_{i+1,j+1}, g_{i+1,j-1}, g_{i,j+1}, g_{i,j-1}, g_{i-1,j+1}, g_{i-1,j-1}, g_{i-1,j}\Big\}. \quad (1)$$

2.1.3 Contrast enhancement using bottom-hat (BH) and top-hat (TH) filtering: To distinguish the background from the cell nuclei effectively, a combination of BH and TH contrast enhancement filtering technique is used [40]. BH is commonly used to filter moderately dark objects from the light background, while TH is on the contrary as displayed in Fig. 1*d*.

The top–bottom hat (TBH) enhancement of grey image A is defined using (2) as:

$$\text{TBH} = A + \text{TH} - \text{BH} \quad (2)$$

where TH is the difference between the grey image A and its opening. BH is the difference between the grey image A and its closing. The opening operation is the collection of foreground parts of an image. Closing operation on the contrary removes small holes.

The above pre-processing steps smoothen and enhance the contrast of the image to prepare it for further analysis.

2.2 Thresholding to identify region of interest

The techniques to identify the region of interest in the literature does not include spatial information and increase the complexity of the technique. Therefore, the energy curve with spatial contextual information of the image is employed to find the tending thresholds. This energy curve reduces the complexity of the technique as described below.

2.2.1 Compute energy curve: The spatial relationship amongst neighbouring pixels of the image A is demonstrated by defining the neighbourhood system N of order d, for (i, j) pixel position as $N_{ij}^d = \{(i+u,\ j+v),\ (u,\ v) \in N^d\}$. The neighbourhood system can assume different configurations according to the value of d [36]. For instance, if the value of $d=2$ then $(u, v) \in \{(\pm 1, 0),\ (0,\ \pm 1),\ (1,\ \pm 1),\ (-1,\ \pm 1)\}$ at (i, j) the spatial position.

The energy curve is generated by considering the spatial information of the image. To generate the energy curve of the image A at grey value g_{ij} $(0 \le g_{ij} \le G)$, firstly a two-dimensional binary matrix is generated as given in (3):

$$\boldsymbol{B}_g = \begin{cases} 1 & g_{ij} > g \\ -1 & g_{ij} < g \end{cases} \quad \forall \{1 \le i \le r, 1 \le j \le s\} \quad (3)$$

Let another matrix $\boldsymbol{C} = \{c_{ij}, 1 \le i \le r, 1 \le j \le s\}$ such that $c_{ij} = 1, \forall (i, j)$. The value of energy E_g of the image A at g grey value is computed using (4):

$$E_g = -\sum_{i=1}^{r}\sum_{j=1}^{s}\sum_{xy \in N_{ij}^2} b_{ij} \cdot b_{xy} + \sum_{i=1}^{r}\sum_{j=1}^{s}\sum_{xy \in N_{ij}^2} c_{ij} \cdot c_{pq}. \quad (4)$$

2.2.2 Obtain the tending thresholds: The image in Fig. 1*d* is further processed to obtain the energy curve so that tending thresholds can be obtained. The energy curve incorporates peaks and valleys, that can be defined in various modes. Every mode has a tending threshold at valley, i.e. in between two adjacent modes which may differentiate the background from objects. The energy curve of the image is smoother than its histogram. This energy curve takes into account the context-sensitive information by including neighbourhood information. This results in better discriminatory capabilities in background and foreground region (cells) of image. The valleys are the tending thresholds say th are $\{6, 104, 197, 227\}$. Here, the valley in each mode of the energy curve represents the tending threshold as shown in Fig. 2.

The threshold values lie in the domain $[0, G]$ where G is the maximum value of grey level. The tending thresholds where energy value is zero will be discarded. Thus, for an instance in Fig. 2, the tending threshold value 6 will be discarded as it has energy zero. Therefore, the tending thresholds to be considered further will be $th = \{104, 197, 227\}$. The flow diagram of the proposed technique is shown in Fig. 3.

2.2.3 Compute the entropy for all the considered tending thresholds and select the threshold with maximum entropy: For each considered tending threshold 'th', Kapur's entropy [37, 41] represented by 'ENT' is computed using (5) and (6):

$$\text{ENT}_{f1} = -\sum_{g=0}^{th} \frac{p_g}{P_{f1}} \log_2\left(\frac{p_g}{P_{f1}}\right), \quad \text{ENT}_{f2} = -\sum_{g=th+1}^{G-1} \frac{p_g}{P_{f2}} \log_2\left(\frac{p_g}{P_{f2}}\right) \quad (5)$$

$$\text{ENT} = \text{ENT}_{f1} + \text{ENT}_{f2} \quad (6)$$

where f_1 and f_2 represent two classes that are the background and the cells (object) in the image, respectively. p_g is the probability of occurrence of grey level g. Here $P_{f1} = \sum_{g=0}^{th} p_g$ and $P_{f2} = 1 - P_{f1}$.

For the considered tending thresholds, i.e. $th = \{104, 197, 227\}$ and $\text{ENT} = \{12.98,\ 11.99,\ 11.38\}$. Now, the entropy at each threshold is calculated and the threshold with maximum entropy is selected. Here, the threshold 104 is selected as it has the maximum entropy value of 12.98. This selected threshold is known as the favourable threshold. All pixels that have the intensity values greater than the favourable threshold value are considered to represent cell nuclei (target region), whereas all pixels that have value in and below the favourable threshold value are considered as background. Thus, the favourable threshold results in effective segmentation of the image.

2.3 Post-processing

The quality of the segmented image may be insufficient for analysis caused by the low signal-to-noise ratio. Thus, the segmented results can be enhanced by applying certain post-processing operations. The different post-processing operations may include dilation, area opening, fill in holes etc.

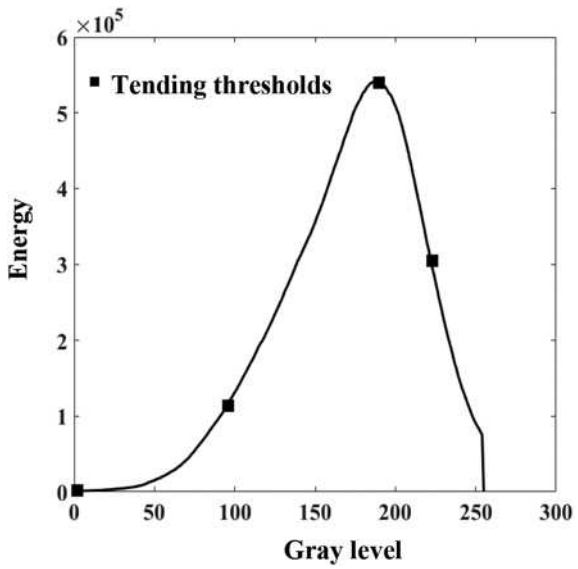

Fig. 2 *Energy curve of the image and its tending thresholds*

This is an open access article published by the IET, Chinese Association for Artificial Intelligence and Chongqing University of Technology under the Creative Commons Attribution -NonCommercial License (http://creativecommons.org/licenses/by-nc/3.0/)

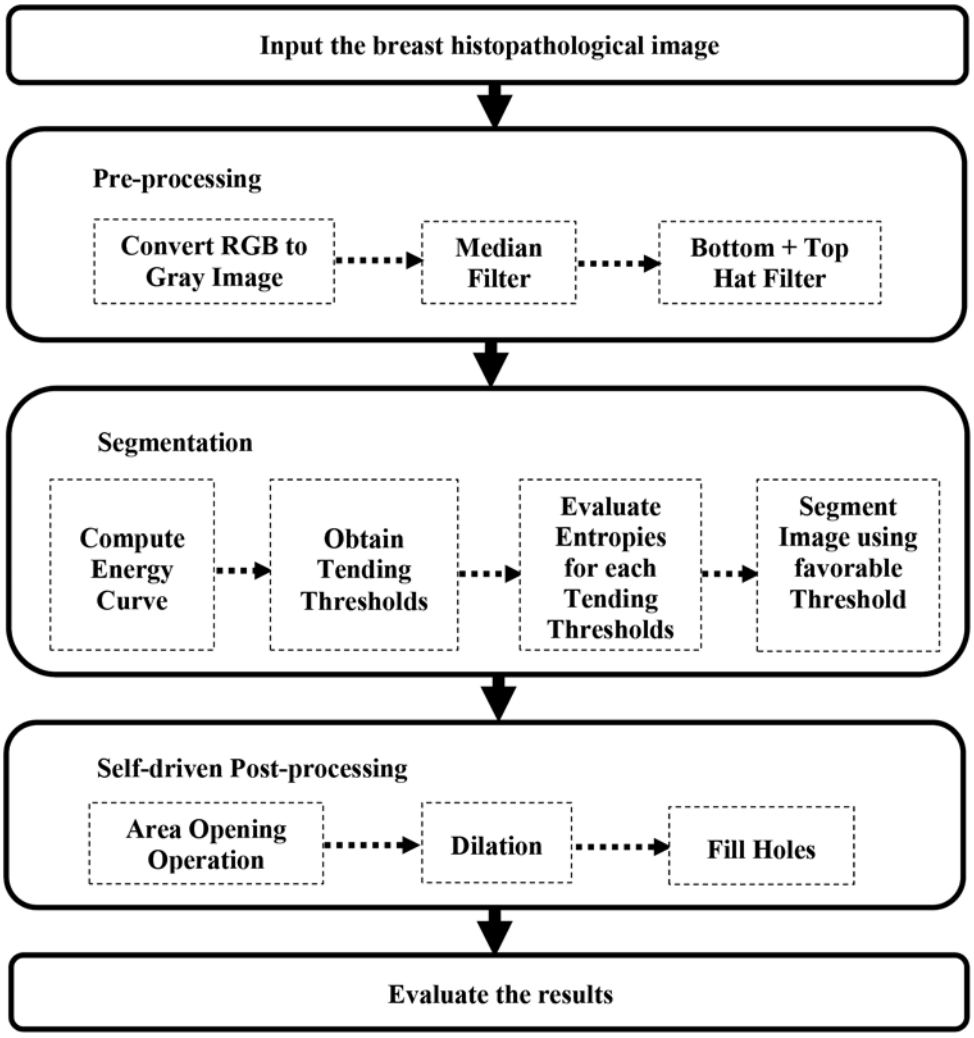

Fig. 3 *Flow diagram of proposed technique*

The different sizes of the structuring element used in morphological operations result in varied segmentation results [23]. The decision about the choice of size of the structuring element, area opening pixels is critical. The fixed value of post-processing operations taken as an input from the user may result in good segmentation results for one image but may vary for other images as the number and area of the size of cells vary for each image in the data set. Therefore, this work proposed self-driven post-processing operations that automatically compute the size of the structuring element and area opening based on the segmented image obtained.

2.3.1 Self-driven area opening operation: The area opening operation will remove the unwanted connected cell nuclei from the breast image. The area corresponds to the number of pixels in the image. The cells with an area less than the specified number of pixel p are removed. For illustration, the reference image in Fig. 4*a* corresponds to the sub-image of the image shown in Fig. 1*d*. To generalise the area operation, an average of the radii of minor and major axis length corresponding to each cell is taken using (7) and (8).

Let n be the number of cells, avg be the average, a_i and b_i be the major axis and minor axis lengths of the cell i, respectively

$$\text{avg_}a = \frac{\sum_{i=1}^{n} a_i}{2n}, \quad \text{avg_}b = \frac{\sum_{i=1}^{n} b_i}{2n} \tag{7}$$

where avg_a and avg_b represent the radii values.

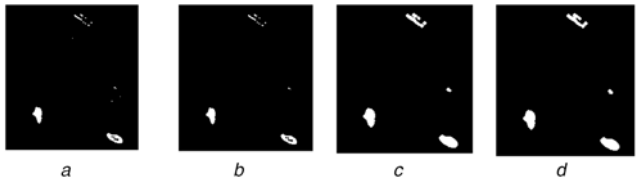

Fig. 4 *Different images obtained during post-processing steps*

a Reference Image (with 13 cells)
b Area opening
c Dilation
d Fill holes

$$p = \text{round}\left(\text{mean}\left(\text{avg_}a, \text{avg_}b\right)\right) \tag{8}$$

where p is the obtained pixel value corresponding to the area.

Illustration: In Fig. 4*a*, where cell number $n = 13$, the area, major axis length and minor axis length for each cell are calculated. Upon calculation, avg_$a = 3.72$ units, avg_$b = 1.72$ units then $p = 3$ units. The cells with an area less than three number of pixels will be removed as shown in bold font in Table 1. Therefore, the value of p obtained will automatically generate the pixel value for the area to be opened resulting in the image with only desirable cells as shown in Fig. 4*b*.

2.3.2 Self-driven size of structuring element for dilation: This operation removes the unconnected dark entities

This is an open access article published by the IET, Chinese Association for Artificial Intelligence and Chongqing University of Technology under the Creative Commons Attribution -NonCommercial License (http://creativecommons.org/licenses/by-nc/3.0/)

Table 1 Statistical illustration of area opening for Fig. 4*a*

Cell No.	Area	Major axis length (a)	Minor axis Length (b)
1	218	24.2287	12.3938
2	**1**	**1.1547**	**1.1547**
3	28	15.8367	2.6548
4	10	5.5833	2.8238
5	3	2.5820	1.7638
6	3	2.5820	1.7638
7	3	2.5820	1.7638
8	5	3.3066	2.1292
9	4	2.3094	2.3094
10	199	28.0469	11.6407
11	**2**	**2.3094**	**1.1547**
12	6	4.9204	2.0578
13	**1**	**1.1547**	**1.1547**

less than the size of structuring element in cell nuclei leaving the background unchanged. A structuring element is a matrix of pixels that describes the neighbourhood used in the processing of each pixel. The appropriate size of the disk-shaped structuring element represented by *se* is computed automatically as explained below:

Once the area opening operation has been applied, the number of cells is reduced to n'. For an instance of Fig. 4*b*, the n' has reduced to ten after the area operation.

Let $l_{\min}$ and $l_{\max}$ be the minimum value of the major axis and maximum value of the minor axis length of the cells present in the image

$$l_{\min} = \min\{a_i\}, \quad l_{\max} = \max\{b_i\} \text{where} \{a_i, b_i\} \forall 1 \le i \le n' \quad (9)$$

$$se = \text{round}\left(\min\left(l_{\min}, l_{\max}\right)\right) \quad (10)$$

In Fig. 4*c*, the values of $l_{\min} = 2.30$ units, $l_{\max} = 12.39$ units and $se = 2$ units which is calculated using equations (9) and (10). So, it can be seen in Fig. 4*c* that the cells are dilated by the structuring element of radii size 2 units. Therefore, an automated size of the structuring element will be calculated for each image which will result in dilation of cells automatically.

2.3.3 Morphological fill operation: Furthermore, the morphological fill hole operation [40] is employed to the image after applying dilation operation, to make the segmentation result less sensitive to the structuring element size. In Fig. 4*d*, the cells with dark pixels within them are filled with holes, where a hole is the region of dark pixels bounded by lighter pixels.

The self-driven post-processing steps increase the structural similarity of cells that improves the qualitative results of the image. This helps in the reduction of overlapping and over-segmentation. As a result, the subject expert can analyse the results more accurately.

3 Experiments and results

The performance of the proposed segmentation technique is evaluated using two publicly available data sets. The first data set includes 50 images of 11 patients. Each H&E stained breast histopathological image and its ground truth is of 512×512-pixel size. The second data set consist of 30 H&E marked 40× magnified images and is provided by the Indian Institute of Technology, Guwahati. Only one image per patient was used and downloaded from The Cancer Genomic Atlas (TCGA) [42] to maximise the nuclear appearance variation. According to the literature, several segmentation techniques are used to detect cancerous cells in breast histopathological images. To confirm the results of the proposed technique, state-of-the-art techniques are used for comparison: FCM, SFCM and SNDRLS. The accuracy of the proposed technique is compared to the deep learning model PangNet [43]. PangNet is a deep learning convolutional architecture that consists of an input layer and an output layer, each of which has one or multiple images, and various convolutional layers that act as intermediate layers that consist of feature maps. The feature maps are also called as the hidden images as these are computed and represented internally by the architecture. The output of each layer acts as an input to the next layer. All these techniques are implemented on images of breast cancer histopathological data sets for comparison with the proposed technique.

To evaluate the effectiveness of the proposed technique, six metrics are used as described in the set of (11–16). These are segmentation accuracy, dice similarity coefficient (DSC), specificity, positive predictive value (PPV) and false positive ratio (FPR) where FN is the false negative that is the cancerous cells detected as non-cancerous, FP is the false positive that is a non-cancerous cell detected as cancerous, TN is the true negative that is a non-cancerous cell detected as non-cancerous cell, TP is the true positive that is a cancerous cell detected as cancerous, and n is the total number of cells in the image. The metrics used for evaluation are specified below.

Segmentation accuracy is the proportion of the correct amount of segmented cells to the total number of cells in an image.

$$\text{Accuracy} = \frac{\text{TP} + \text{TN}}{n} \times 100. \quad (11)$$

Specificity is the measure of the percentage of healthy cells that are correctly identified as non-cancerous

$$\text{Specificity} = \frac{\text{TN}}{\text{TN} + \text{FP}} \times 100. \quad (12)$$

DSC is the overlap measure between the segmented image and ground truth image

$$\text{DSC} = \frac{2\text{TP}}{2\text{TP} + \text{FP} + \text{FN}}. \quad (13)$$

PPV is the amount of the number of positive results

$$\text{PPV} = \frac{\text{TP}}{\text{FP} + \text{TP}}. \quad (14)$$

FPR is the number of non-cancerous cells identified as cancerous cells.

$$\text{FPR} = \frac{\text{FP}}{\text{FP} + \text{TN}}. \quad (15)$$

Standard error of mean (SEM) is used to calculate any significance in the deviation of the mean [44]

$$\text{SEM} = \frac{\sigma}{\sqrt{m}} \quad (16)$$

where σ is the standard deviation of the total data and m is the total number of images.

The average results of four quantitative metrics: FPR, DSC, PPV, and specificity are presented in Table 2. Higher the value of DSC, higher is the similarity index of the cancerous breast cells extracted. Lower the rate of FPR, fewer are the false cells segmented. Therefore, increase in DSC value for the proposed technique verifies that it outperforms with significant results.

It can be observed from Table 2 that PPV for the proposed technique is improved by 9% for data set 1 and 1.5% (approximately) for data set 2, whereas specificity is improved by 3% approximately for both the data sets. It can also be observed that the standard mean error has been reduced significantly for all the evaluation metrics for both the data sets which prove that the proposed technique outperforms. The quantitative results presented in Table 3, for data set 1 and data set 2, show that the accuracy for

This is an open access article published by the IET, Chinese Association for Artificial Intelligence and Chongqing University of Technology under the Creative Commons Attribution -NonCommercial License (http://creativecommons.org/licenses/by-nc/3.0/)

Table 2 Average results of different benchmarks for proposed and existing state-of-the-art techniques

	Metrics	FCM	SFCM	SNDRLS	Proposed technique
Data set #1	FPR	3.65 ± 0.80	2.12 ± 0.22	2.99 ± 0.36	**1.16 ± 0.20**
	DSC	50.4 ± 2.52	49.8 ± 2.27	49.9 ± 1.98	**60.6 ± 1.29**
	PPV	66.8 ± 0.04	69.1 ± 0.03	74.1 ± 2.16	**83.4 ± 0.02**
	Specificity	93.4 ± 1.08	94.6 ± 0.92	93.7 ± 0.96	**97.5 ± 0.29**
Data set #2	FPR	5.34 ± 0.60	6.37 ± 0.44	7.19 ± 0.51	**2.87 ± 0.32**
	DSC	77.9 ± 2.11	79.3 ± 2.01	73.5 ± 2.12	**79.8 ± 1.91**
	PPV	83.2 ± 0.99	81.4 ± 0.87	77.9 ± 1.43	**84.7 ± 0.66**
	Specificity	94.6 ± 0.88	93.6 ± 0.73	92.8 ± 0.98	**97.1 ± 0.45**

Bold values indicates effectiveness of the proposed technique

Table 3 Comparison of accuracy and SEM of proposed technique with traditional and deep learning based state-of-the-art techniques

	Data set #1		Data set #2	
Metrics	Accuracy, %	SEM	Accuracy, %	SEM
FCM	88.5	1.42	89.0	1.35
SFCM	89.8	1.01	89.3	1.21
SNDRLS	90.2	1.20	90.8	1.10
PangNet	92.4	1.00	91.8	0.97
proposed	**93.1**	**0.81**	**93.5**	**0.35**

Bold values indicates effectiveness of the proposed technique

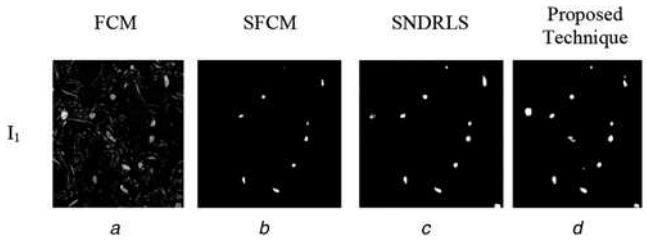

Fig. 5 *Segmented images obtained by the proposed technique and the state-of-the-art techniques with respect to I_1 image*

a (FCM)
b SFCM
c SNDRLS
d Proposed technique

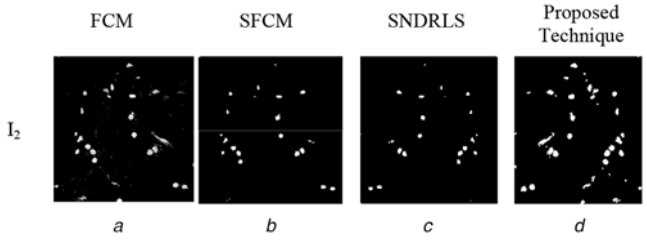

Fig. 6 *Segmented images obtained by the proposed technique and the state-of-the-art techniques with respect to I_2 image*

a (FCM)
b SFCM
c SNDRLS
d Proposed technique

the proposed technique has been improved by 1% irrespective of the data set used. For accuracy, measure the standard error has been reduced on by 24% for data set 1 and 64% for data set 2 in comparison to state-of-the-art techniques. Hence, the performance of the proposed technique is efficient than the existing state-of-the-art techniques. This proves that the proposed technique can effectively detect cancerous cells from histopathological breast images.

The qualitative performance evaluation for the segmented images acquired by the proposed and state-of-the-art techniques for two

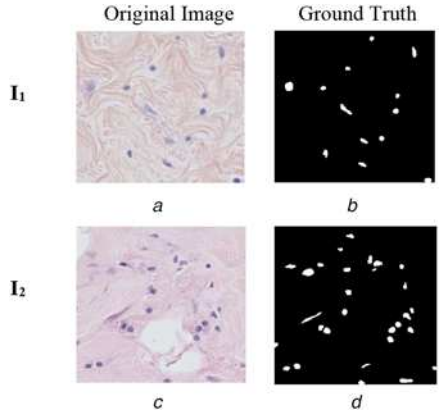

Fig. 7 *Original histopathological image and the relative ground truth image*

a Original Image I_1
b Ground Truth of I_1
c Original Image I_2
d Ground Truth of I_2

images annotated by I_1 and I_2 are shown in Figs. 5 and 6, respectively. The original images, i.e. the histopathological image of the breast are represented in Figs. 7*a* and *c* and their corresponding ground truth are displayed in Figs. 7*b* and *d* for two different image cases from the employed data set.

The comparison of qualitative results for the proposed technique and the state-of-the-art techniques is done with respect to the ground truth images shown in Figs. 7*b* and *d*. Figs. 5*a* and 6*a* depict that due to high contrast and weak edges, many false cell regions are segmented by FCM. These cells are joined to false foregrounds and misinterpreted as cancerous cells. In addition, Figs. 5*b* and *c* represent that the cells are not accurately segmented by SFCM and SNDRLS techniques, respectively. The cells are fused by dark regions in the background in Figs. 6*b* and *d*. Several cells are neglected out while segmentation is done using SNDRLS, hence resulting in loss of important information. The selection of a favourable threshold avoids the cells from being connected to any ambiguous boundary. The proposed technique smoothens the obscure background and segments the cell boundary clearly by applying proposed self-driven post-processing operations.

In Fig. 5, for image I_1, the FPR for FCM is 4.18%, SFCM is 0.86%, SNDRLS is 0.21%, and 0.01% for the proposed technique with respect to ground truth in Fig. 7*b*. The reduction in FPR for the proposed technique verifies that it is more efficient as it reduces false segmentation. As evident from Figs. 5*d* and 6*d*, the segmentation results achieved by the proposed technique are relatively very close to its ground truth image in Figs. 7*b* and *d*, respectively.

Processing one image of size 512 × 512 pixels took an average of 6.10 s for FCM, 7.72 for SFCM, 5.62 s for SNDRLS, 6.11 s for PangNet, and 4.82 s for the proposed technique. The computational time is independent of the number of cells and is estimated on Windows 10 (64-bit) operating system with MATLAB R2017a tool.

This is an open access article published by the IET, Chinese Association for Artificial Intelligence and Chongqing University of Technology under the Creative Commons Attribution -NonCommercial License (http://creativecommons.org/licenses/by-nc/3.0/)

4 Conclusion

This work proposes an automated segmentation technique followed by completely self-driven post-processing operations. Automated threshold selection reduces the need for initial level set, time step, weighted area coefficient parameters setting. The proposed segmentation technique considers the neighbourhood information present in the image using the energy curve. The energy curve is much smoother than histogram and it helps in selecting the favourable threshold automatically. Based on the segmentation results, the self-driven post-processing operations automatically determine the values of parameters for area opening and dilation, which is time-consuming for an expert/radiologist. The proposed technique has several advantages over the state-of-the-art techniques: (i) spatial information is incorporated; (ii) no prior setting of any initial parameter; (iii) independent of magnification; and (iv) automatically determines the inputs for morphological operations to enhance image based on segmented cell nuclei of the image. This leads to enhancement in segmentation by identifying the cancerous cells accurately. The results achieved by the proposed technique are evaluated and compared with the four state-of-the-art techniques to measure its effectiveness. Experimental results of different metrics using two different data sets of breast histopathological images confirmed the effectiveness of the proposed technique.

In the future, the experts may utilise the results of the proposed technique to perform cell classification which would be very advantageous for pathologists/experts. Furthermore, this approach can be prolonged to other organs in a similar pathology for segmentation and classification of cancerous cells. Automatic and self-driven morphological operations to enhance the segmented results can help the subject expert to make early or more accurate prognosis as well as diagnosis.

5 References

[1] Hayakawa, T., Prasath, V.S., Kawanaka, H., *et al.*: 'Computational nuclei segmentation methods in digital pathology: a survey', *Arch Comput Meth. Eng.*, 2019, **26**, p. 1

[2] Cahill, L.C., Fujimoto, J.G., Giacomelli, M.G., *et al.*: 'Comparing histologic evaluation of prostate tissue using nonlinear microscopy and paraffin H&E: a pilot study', *Mod. Pathol.*, 2019, **32**, (8), pp. 1158–1167

[3] Veta, M., Pluim, J.P., Van Diest, P.J., *et al.*: 'Breast cancer histopathology image analysis: a review', *IEEE Trans. Biomed. Eng.*, 2014, **61**, (5), pp. 1400–1411

[4] Aswathy, M.A., Jagannath, M.: 'Detection of breast cancer on digital histopathology images: present status and future possibilities', *Inform. Med. Unlocked*, 2017, **8**, pp. 74–79

[5] 'Cancer', Available at https://www.who.int/news-room/factsheets/ detail/cancer, accessed May 2, 2019

[6] Das, A., Nair, M.S., Peter, S.D.: 'Computer-aided histopathological image analysis techniques for automated nuclear atypia scoring of breast cancer: a review', *J. Digit. Imaging*, 2020, **33**, pp. 1–31

[7] Irshad, H., Veillard, A., Roux, L., *et al.*: 'Methods for nuclei detection, segmentation, and classification in digital histopathology: a review – current status and future potential', *IEEE Rev. Biomed. Eng.*, 2014, **7**, pp. 97–114

[8] Jothi, J.A.A., Rajam, V.M.A.: 'A survey on automated cancer diagnosis from histopathology images', *Artif. Intell. Rev.*, 2017, **48**, (1), pp. 31–81

[9] Kaushal, C., Koundal, D., Singla, A.: 'Comparative analysis of segmentation techniques using histopathological images of breast cancer'. IEEE 3rd Int. Conf. on Computing Methodologies and Communication (ICCMC), Erode, Tamil Nadu, India, 2019, pp. 261–266

[10] He, L., Long, L.R., Antani, S., *et al.*: 'Histology image analysis for carcinoma detection and grading', *Comput. Methods Programs Biomed.*, 2012, **107**, (3), pp. 538–556

[11] Taheri, S., Fevens, T., Bui, T.D.: 'Robust nuclei segmentation using statistical level set method with topology preserving constraint', in: Ayman, E-B, Suri, J.S. (Eds). 'Level set method in medical imaging segmentation' (CRC Press, USA, 2019), pp. 71–98

[12] Vishnoi, S., Jain, A.K., Sharma, P.K.: 'An efficient nuclei segmentation method based on roulette wheel whale optimization and fuzzy clustering', *Evol. Intell.*, 2019, **12**, pp. 1–12

[13] Wang, H., Roa, A.C., Basavanhally, A.N., *et al.*: 'Mitosis detection in breast cancer pathology images by combining handcrafted and convolutional neural network features', *J. Med. Imag.*, 2014, **1**, (3), pp. 1–8

[14] Kowal, M., Filipczuk, P., Obuchowicz, A., *et al.*: 'Computer-aided diagnosis of breast cancer based on fine needle biopsy microscopic images', *Comput. Biol. Med.*, 2013, **43**, (10), pp. 1563–1572

[15] Abdolhoseini, M., Kluge, M.G., Walker, F.R., *et al.*: 'Segmentation of heavily clustered nuclei from histopathological images', *Sci. Rep.*, 2019, **9**, (1), p. 4551

[16] Mouelhi, A., Sayadi, M., Fnaiech, F., *et al.*: 'Automatic image segmentation of nuclear stained breast tissue sections using color active contour model and an improved watershed method', *Biomed. Signal Proc. Control*, 2013, **8**, (5), pp. 421–436

[17] Ali, S., Madabhushi, A.: 'An integrated region-, boundary-, shape-based active contour for multiple object overlap resolution in histological imagery', *IEEE Trans. Med. Imaging*, 2012, **31**, (7), pp. 1448–1460

[18] Xu, J., Gong, L., Wang, G., *et al.*: 'Convolutional neural network initialized active contour model with adaptive ellipse fitting for nuclear segmentation on breast histopathological images', *J. Med. Imag.*, 2019, **6**, (1), p. 017501

[19] Sornapudi, S., Stanley, R.J., Stoecker, W.V., *et al.*: 'Deep learning nuclei detection in digitized histology images by superpixels', *J. Pathol. Inform.*, 2018, **9**, (5), p. 5

[20] Plissiti, M.E., Nikou, C., Charchanti, A.: 'Automated detection of cell nuclei in pap smear images using morphological reconstruction and clustering', *IEEE Trans. Inf. Technol. Biomed.*, 2011, **15**, (2), pp. 233–241

[21] Mittal, H., Saraswat, M.: 'An automatic nuclei segmentation method using intelligent gravitational search algorithm based superpixel clustering', *Swarm. Evol. Comput.*, 2019, **45**, pp. 15–32

[22] Wang, P., Hu, X., Li, Y., *et al.*: 'Automatic cell nuclei segmentation and classification of breast cancer histopathology images', *Signal Process.*, 2016, **122**, pp. 1–13

[23] Veta, M., Van Diest, P.J., Kornegoor, R., *et al.*: 'Automatic nuclei segmentation in h&e stained breast cancer histopathology images', *PloS One*, 2013, **8**, (7), pp. 1–12

[24] Qu, A., Chen, J., Wang, L., *et al.*: 'Two-step segmentation of hematoxylin-eosin stained histopathological images for prognosis of breast cancer'. IEEE Int. Conf. on Bioinformatics and Biomedicine (BIBM), Belfast, UK, 2014, pp. 218–223

[25] Vahadane, A., Sethi, A.: 'Towards generalized nuclear segmentation in histological images'. IEEE 13th Int. Conf. on Bioinformatics and Bioengineering (BIBE), Chania, Greece, 2013, pp. 1–4

[26] Husham, A., Hazim Alkawaz, M., Saba, T., *et al.*: 'Automated nuclei segmentation of malignant using level sets', *Microsc. Res. Tech.*, 2016, **79**, (10), pp. 993–997

[27] Zhao, L., Wan, T., Feng, H., *et al.*: 'Improved nuclear segmentation on histopathology images using a combination of deep learning and active contour model'. Int. Conf. on Neural Information Processing, Cham, 2018, pp. 307–317

[28] Gubarkova, E.V., Sovetsky, A.A., Zaitsev, V.Y., *et al.*: 'OCT-elastography-based optical biopsy for breast cancer delineation and express assessment of morphological/molecular subtypes', *Biomed. Opt. Express*, 2019, **10**, (5), pp. 2244–2263

[29] Koundal, D., Gupta, S., Singh, S.: 'Automated delineation of thyroid nodules in ultrasound images using spatial neutrosophic clustering and level set', *Appl. Soft Comput.*, 2016, **40**, pp. 86–97

[30] Li, Z., Tao, R., Wu, Q., *et al.*: 'DA-RefineNet: A dual input WSI image segmentation algorithm based on attention', arXiv preprint arXiv:1907.06358, 2019

[31] Mejbri, S., Franchet, C., Reshma, I.A., *et al.*: 'Deep analysis of CNN settings for new cancer whole-slide histological images segmentation: the case of small training sets'. 6th Int. Conf. on BioImaging (BIOIMAGING), Prague, Czech Republic, 2019, pp. 120–128

[32] Kaushal, C., Bhat, S., Koundal, D., *et al.*: 'Recent trends in computer assisted diagnosis (CAD) system for breast cancer diagnosis using histopathological images', *IRBM*, 2019, **40**, (4), pp. 211–227

[33] Pan, X., Li, L., Yang, H., *et al.*: 'Accurate segmentation of nuclei in pathological images via sparse reconstruction and deep convolutional networks', *Neurocomputing*, 2017, **229**, pp. 88–99

[34] Chekkoury, A., Khurd, P., Ni, J., *et al.*: 'Automated malignancy detection in breast histopathological images'. Medical Imaging 2012: Computer-Aided Diagnosis, Int. Society for Optics and Photonics, San Diego, CA, USA, 2012, 8315, p. 831515

[35] Krishnan, M.M.R., Venkatraghavan, V., Acharya, U.R., *et al.*: 'Automated oral cancer identification using histopathological images: a hybrid feature extraction paradigm', *Micron*, 2012, **43**, (2–3), pp. 352–364

[36] Rezaei, S., Emami, A., Karimi, N., *et al.*: 'Gland segmentation in histopathological images by deep neural network', arXiv preprint arXiv: 1911. 00909, 2019

[37] Singla, A., Patra, S.: 'A fast automatic optimal threshold selection technique for image segmentation', *Signal. Image. Video. Process.*, 2017, **11**, (2), pp. 243–250

[38] Available at http://cbio.mines-paristech.fr/-pnaylor/BNS.zip, accessed March 2018

[39] Available at https://monuseg.grand-challenge.org/Data/, accessed April 2018

[40] Bustacara-Medina, C., Flórez-Valencia, L.: 'An automatic stopping criterion for contrast enhancement using multi-scale top-hat transformation', *Sens. Imaging.*, 2019, **20**, (1), p. 26

[41] Hinojosa, S., Dhal, K.G., Elaziz, M.A., *et al.*: 'Entropy-based imagery segmentation for breast histology using the stochastic fractal search', *Neurocomputing*, 2018, **321**, pp. 201–215

[42] Available at https://www.cancer.gov/about-nci/organization/ccg/research/structural-genomics/tcga, accessed April 2018

[43] Naylor, P., Lae, M., Reyal, F., *et al.*: 'Nuclei segmentation in histopathology images using deep neural networks'. IEEE 14th Int. Symp. on Biomedical Imaging (ISBI), Melbourne, Australia, 2017, pp. 933–936

[44] Ishwaran, H., Lu, M.: 'Standard errors and confidence intervals for variable importance in random forest regression, classification, and survival', *Stat. Med.*, 2019, **38**, (4), pp. 558–582

This is an open access article published by the IET, Chinese Association for Artificial Intelligence and Chongqing University of Technology under the Creative Commons Attribution -NonCommercial License (http://creativecommons.org/licenses/by-nc/3.0/)